Application of pulsed laser annealing to ferromagnetic GaMnAs

Danilo Bürger,[1,*] Shengqiang Zhou,[1] Mukesh Pandey,[2] Chebolu Subrahmanya Viswanadham,[3] Jörg Grenzer,[1] Olga Roshchupkina,[1] Wolfgang Anwand,[1] Helfried Reuther,[1] Volker Gottschalch,[4] Manfred Helm,[1] and Heidemarie Schmidt[1]

[1]*Institute of Ion Beam Physics and Materials Research, Forschungszentrum Dresden-Rossendorf, P.O. Box 510119, 01314 Dresden, Germany*

[2]*High Pressure and Synchrotron Radiation Physics Division, Bhabha Atomic Research Centre, Mumbai 400085, India*

[3]*Materials Science Division, Bhabha Atomic Research Centre, Mumbai 400085, India*

[4]*Institut für Anorganische Chemie, Fakultät für Chemie und Mineralogie, Universität Leipzig, Linnéstraße 3, 04103 Leipzig, Germany*

(Received 24 September 2009; revised manuscript received 28 January 2010; published 2 March 2010)

In this experimental and theoretical work we focus on the technique of pulsed laser annealing applied to the metastable ferromagnetic semiconductor GaMnAs. Analytical heat-flow calculations are used to illustrate the position and time-dependent temperature distribution during the whole laser annealing process. Such heat-flow calculations will also play an indispensable role for the preparation of other new metastable diluted ferromagnetic semiconductors by ion implantation and subsequent laser annealing. The structural, magnetic, and magnetotransport properties of ferromagnetic GaMnAs have been probed in dependence on the annealing parameters, e.g., the number of laser pulses and the pulse length. Annealing with a single KrF laser pulse of 30 ns and 0.26 J/cm^2 with the photon energy above the GaAs band gap energy leads to similar magnetic properties like annealing with a single 3 ns Nd:YAG laser pulse with the photon energy below the GaAs band gap energy. We observed that possibly due to Mn diffusion and decreasing hole concentration, several laser pulses degrade the structural and magnetic properties of GaMnAs. Our results reveal the largest saturation magnetization in Mn-implanted GaAs annealed with a single KrF laser pulse.

DOI: 10.1103/PhysRevB.81.115202 PACS number(s): 66.30.Xj, 72.20.Dp, 72.20.My, 72.25.Dc

I. INTRODUCTION

Apart from low-temperature molecular beam epitaxy, ion implantation is an alternative nonequilibrium method to introduce several orders more Mn into GaAs than under solid equilibrium conditions. However, the activation of dopant atoms after ion implantation can only be achieved by post-annealing. Rapid thermal annealing (RTA) above the growth temperature of low-temperature molecular beam epitaxy (LT-MBE) grown samples leads to the formation of secondary phases in GaMnAs.[1] For Mn-implanted GaAs conventional RTA on a time scale of several seconds leads to the formation of MnAs particles.[2] In Ref. 3 we reported about Mn-implanted GaAs followed by flash lamp annealing (FLA) on the ms time scale resulting in low Curie temperatures and small magnetic moments. The pulsed laser annealing on a time scale of nanoseconds is the only effective technique to fabricate a metastable diluted magnetic semiconductor (DMS) from Mn-implanted GaAs (Ref. 4) or GaP.[5] During PLA, the near-surface region of the material melts, solidifies epitaxially, and cools down within several microseconds. Scarpulla *et al.* reported that Mn-implanted GaAs has a Curie temperature between 29 and 130 K depending on the concentration of Mn ions and on the applied PLA parameters.[4,6] All samples exhibit the characteristic signatures of diluted ferromagnetic GaMnAs grown by LT-MBE, such as magnetotransport effects,[6–8] nonmagnetic compensation by *n*-type dopants,[9] magnetic anisotropy,[10] passivation by hydrogen,[11] as well as the strong magnetic circular dichroism at the Mn $L_{2,3}$ edge.[12] Note that the fast cooling rate of PLA, namely up to 10^{11} K/s, prevents the diffusion and therefore the formation of secondary phases. As an advantage of ion implantation, the lateral structuring can be easily done by combining with lithography[13] and by optical near-field irradiation.[11] This opens the way to fabricate nanostructured diluted magnetic semiconductors.

Despite the success in fabricating ferromagnetic GaAs:Mn by PLA, to the best of our knowledge, there is no significant increase in the Curie temperature compared to LT-MBE grown GaAs:Mn. However, the explorable PLA parameter space is very large and may be optimized with regards to the fabrication of metastable diluted magnetic semiconductors. Indeed, PLA has been used to activate implanted dopants in semiconductors, e.g., Si (Ref. 14) and Ge.[15] The heat-flow calculation for Si has been presented in Refs. 16 and 17. A review on the interaction between laser light and solid materials has been given by Allmen.[18] The maximum free carrier concentration in Si or Ge implanted by electrical dopants, e.g., group III and V elements, followed by PLA amounts to 10^{21} cm^{-3}.[14] By optimizing the PLA parameters, it is expected that a large hole concentration may be realized in Mn-implanted GaAs. Note that the Curie temperature of GaAs:Mn is proportional to the amount of substituted Mn ions and to the hole concentration[19] and that the recrystallization and dopant activation strongly depend on the PLA parameters. In this paper, we present a semianalytical heat-flow model to visualize the cooling process of Mn-implanted GaAs after PLA. The calculation can well predict the energy threshold for recrystallization. One-dimension-like pulsed laser annealing is proposed to effectively decrease the cooling time and thus also possible Mn clustering and Mn acceptor deactivation. We varied the PLA parameters, e.g., the pulse duration and the pulse number, within our experimental facilities to obtain a more complete picture of the influence of the PLA parameters on the sample properties.

TABLE I. Energy and fluence of Mn^+ ions used to implant 3 and 6 at. % Mn into GaAs.

Energy (keV)	Fluence 3 at. % (10^{15} cm^{-2})	Fluence 6 at. % (10^{15} cm^{-2})
150	7	17
300	27	55

The paper is organized as follows. We present the sample fabrication and briefly describe the applied experimental methods in Sec. II

The heat-flow calculations and possible improvements of the PLA technique are discussed in Sec. III. To fill a lack of the literature of the 80s we will also report time-dependent temperature profiles during and after a single laser pulse and reveal large differences in the cooling rate for one-dimensional stripe annealing and two-dimensional homogenous annealing. This may be of interest for processing materials containing fast diffusing dopant atoms.

In Sec. IV the structural properties of GaMnAs will be presented. A probed recrystallization depth of ca. 170 nm is supported by modeling Rutherford backscattering spectrometry/channeling (RBS/C) and positron annihilation spectroscopy (PAS) data. The high resolution x-ray diffraction (HR-XRD) pattern reveal an overcompensation of the GaMnAs lattice after ten laser pulses. This effect is attributed to randomly compressively strained crystallites inside a dislocation network.

In Sec. V the magnetic properties of GaMnAs samples annealed under different conditions will be discussed. We present the degraded magnetic properties in Mn-implanted GaAs after ten pulses, namely a reduced Curie temperature, coercivity and saturation magnetization. The superconducting quantum interference device (SQUID) and Hall effect measurement data reveal good agreement between hysteretic magnetization and magnetotransport properties, respectively.

Finally, we conclude the paper and show how heat-flow calculations may be used for the preparation of new diluted ferromagnetic semiconductors by ion implantation and subsequent annealing.

II. SAMPLE FABRICATION AND EXPERIMENT

Ca. 1 μm thick GaAs films have been grown by metal-organic vapor phase epitaxy (MOVPE) on (001)-GaAs substrates with a *p*-doping level of 1.5×10^{16} cm^{-3} Zn atoms. The Mn implantation was carried out at room temperature at an angle of 7° to prevent channeling effects. The current density was 0.75 μA cm^{-2}. In Table I the energy and fluences of Mn ions used for implantation are indicated. The implantation with multi-energy ions results in a boxlike Mn profile over a depth of 300 nm.

After implantation we annealed the samples with a KrF excimer laser (248 nm) with a pulse duration of around 30 ns or with a Nd:YAG solid state laser (1064 nm) with a shorter pulse length of around 3–5 ns. We also increased the number of laser pulses to ten and 100 and investigated possible cluster formation being known from LT-MBE GaMnAs samples that are heated up over their growth temperature on a longer time scale.[20–23]

The effective laser energy irradiation per pulse on the sample from the COMpex KrF excimer laser from Lambda Physik was 130 mJ. For samples annealed with more than one pulse, the repetition rate was 1 Hz. Note that with respect to the cooling rate 1 s is sufficient to thermalize the samples at room temperature and no smaller repetition rate had to be chosen. The KrF laser pulse was homogeneously expanded to around 0.5 cm^2 (two-dimensional annealing). The Nd:YAG solid state laser EKSPLA NL-301 HT had a Gaussian energy distribution with an FWHM diameter of around 4 mm. The pulse energy of 110 or 140 mJ hit the samples with a spot diameter of around 3 mm. Note, that the Nd:YAG photon energy lies below the band gap of GaAs. The KrF excimer laser melted the implanted GaMnAs layer up to a depth of around 170 nm. Therefore, the liquid phase epitaxy did not start from the unimplanted crystalline GaAs bulk material. High-resolution transmission electron microscopy (HRTEM) images reveal some poly crystals with a size of 30 nm near the maximum melting depth and a high crystalline quality with some dislocation lines near the surface. We do not find hints for explosive recrystallization like reported for laser annealed Si in Ref. 24.

Using structural and magnetic characterization methods, we elucidated the recrystallization depth and the redistribution of Mn ions after PLA, as well as the corresponding magnetic and transport properties. The RBS/C spectra were collected with a collimated 1.7 MeV He^+ beam at a backscattering angle of 170°. For that, the samples were mounted on a three-axis goniometer with a precision of 0.01°. Depth profiling by Auger electron spectroscopy was performed with a scanning Auger electron spectrometer Microlab 310F (Fisons Instruments). PAS measurements have been performed with monoenergetic positrons with a beam spot diameter of 4 mm under high vacuum conditions at an accelerator voltage from 30 V to 36 kV. HR-XRD measurements were carried out using a high resolution setup (GEXRD3003HR). Magnetic properties were obtained by SQUID magnetometry down to 3 K using a MPMS XXL 7 T system from Quantum Design. Magnetotransport measurements were carried out in van-der-Pauw geometry with an Hall effect measurement system 9700A from Lakeshore between 5 and 300 K.

III. HEAT-FLOW CALCULATIONS

In this section the calculated heat flow during a whole laser annealing process of Mn-implanted GaAs will be discussed. First we show the sample temperature in dependence on the distance from the surface and on the time after the PLA pulse. Then, the heat-flow for the special case of one-dimensional annealing, e.g., by scanning a stripelike laser beam as narrow as few μm over the sample, will be discussed in detail. The presented heat-flow calculations neglect enthalpy changes during melting and recrystallization and will not reach the high accuracy of analytical approaches applied to Si in the 80s. Here we intend to give the reader a

tool for estimating the optimal energy density for PLA applied to new metastable ferromagnetic semiconductors. This approach is reasonable because more accurate numerical calculations need more detailed material parameters that are not available for most "exotic" materials.

The annealing of GaAs with lasers, electrons, and ions is reviewed in Ref. 25. Flash lamp annealing on the ms time scale produces a GaMnAs DMS with a very low Curie temperature.[3] Laser annealing with a pulse duration as short as ns is successful in the preparation of GaMnP (Ref. 5) or GaMnAs (Ref. 6) DMS. The success stands on the very short pulse and the high power density of the laser. This results in a melting of the implanted layer. The solubility of magnetic dopant atoms in the liquid phase is much higher than in the solid phase.[26] During the epitaxial regrowth the magnetic dopants are incorporated over their room temperature solubility limit in the solid phase. Higher regrowth velocities result in a higher incorporation of magnetic dopant atoms. The maximum regrowth velocity of the liquid/solid interface should be around twice the diffusive transport velocity.[27] Depending on the ratio $k=C_S/C_L$ between the solubility in the solid (C_S) and in the liquid phase (C_L), for low values of k an accumulation of dopants near the liquid/solid interface in the liquid phase occurs. This regrowth mechanism is responsible for the experimentally observed surface segregation of the implanted ions. Furthermore, secondary phases are formed when the concentration of dopants near the liquid/solid interface in the liquid phase lies over the eutectic concentration.

For a better understanding of the temperature profile in PLA samples, we performed heat-flow calculations for one KrF laser pulse with a pulsed laser energy density of 260 mJ cm^{-2}. Equation (1) represents the one-dimensional heat transfer equation for the applied homogeneous two-dimensional annealing. This equation is valid without external heat sources. It is a partial differential equation of parabolic character,

$$\frac{\partial}{\partial t}u(x,t) = a \cdot \frac{\partial^2}{\partial x^2}u(x,t), \tag{1}$$

where $u(x,t)$ can be interpreted as a scalar temperature field in the sample that depends on time t and position x normal to the sample surface. a is the thermal diffusion coefficient being related with the heat conductivity Λ, mass density ρ, and heat capacitance c_p as follows:

$$a = \frac{\Lambda}{\rho c_p}. \tag{2}$$

We used a value of $a=26.5\times10^{-6}$ m^2 s^{-1} for crystalline GaAs. The thermal diffusion length L can be estimated by $L=\sqrt{4at}$. For a typical pulse duration of $t=20$ ns the thermal diffusion length amounts to $L=1.78$ μm. Note that this value is only valid for an infinitesimal short pulse where all the energy is deposited immediately ($t=0$) at the sample surface ($x=0$). The time-dependent power density of the KrF excimer laser varies over 40 ns. Therefore, a more detailed heat-flow calculation, e.g., using Green's functions, yields the time-dependent temperature profile during the laser pulse.

The 1-dimensional Green function of a δ-function-like temperature profile in a homogeneous medium with a constant thermal diffusion coefficient a for $x\in(-\infty\ldots+\infty)$ is given by

$$G_0(x,t) = \frac{1}{\sqrt{4\pi at}}\exp\left(\frac{-x^2}{4at}\right). \tag{3}$$

We have to consider two different materials, ambient air and GaAs with the sample surface at $x=0$. The thermal diffusion coefficient of air amounts to $a_{air}\approx20\times10^{-6}$ m^2 s^{-1} and is comparable to the thermal diffusion coefficient of GaAs. Therefore, the heat transfer in air and GaAs is similar and Eq. (1) also holds in air. Note that the energy flow from $x=0$ into the ambient air can be neglected because of the low heat capacitance of air.

Now, with the Green's function from Eq. (3) it is possible to solve the heat transfer Eq. (1) for arbitrary time and position dependent sources. Using a time-dependent source function $Q(x,t)=\delta(x-x_0)f(t)$ the solution of Eq. (1) can be written in the form

$$u(x,t) = \int d^3x' \int_{-\infty}^{t} Q(x',t')G_0(x-x',t-t')dt'. \tag{4}$$

If we assume that the energy is deposited at $x_0=0$ and that the laser pulse starts at t=0, Eq. (4) simplifies to

$$u(x,t) = \int_0^t f(t')G_0(x,t-t')dt'. \tag{5}$$

The function $f(t')$ is proportional to the laser power density. Because it is not easy to expand the laser power in a simple function, here we discretize $f(t')$ and obtain the temperature distribution in the PLA sample after 42 ns in time steps of 2 ns as follows:

$$u(x,t=42\ \text{ns}) = \sum_{t_i=0\ \text{ns}}^{40\ \text{ns}} f_i G_0(x,t-t_i). \tag{6}$$

Later, the discretized sequence f_i will be normalized so that the temperature profile matches the deposited energy of 130 mJ.

The results of the heat-flow calculations for the KrF laser are presented in Fig. 1. The inset shows the profile of the laser pulse. It is visible that after around 20 ns the melting temperature is reached at the surface. For $t\geq20$ ns the calculated temperature near the surface is not correct, because the value of the melting enthalpy of crystalline GaAs of 729 Jg^{-1} that should be smaller for amorphous materials, was neglected. Therefore, the complete melting depth of around 400 nm after 42 ns, i.e., after the laser pulse, is overestimated. If we calculate the melting depth from the energy in the power profile ranging from 20 ns to 40 ns (60 mJ), we obtain a value of around 250 nm (not shown here). Because of the strong energy flow inside the sample and a high reflection above 60 % in the liquid phase (estimated), this value is also an overestimation. From RBS measurements (shown later) the melting depth amounts to 150 nm, i.e., the thickness of the melted and recrystallized layer is smaller than the thickness of the implanted layer.

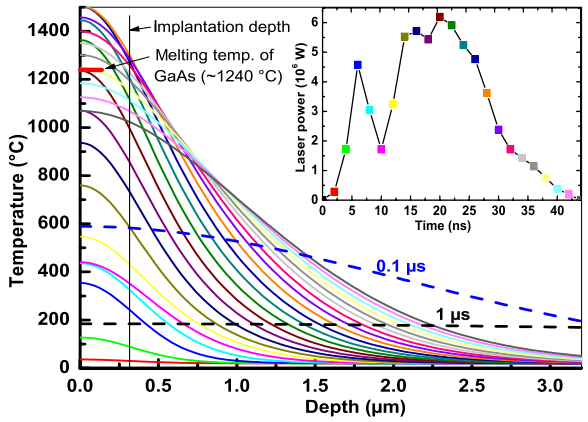

FIG. 1. (Color online) Calculated temperature profile for various times identified by the inset during the single laser pulse (solid) and after 0.1 μs and 1 μs (scattered). The melting temperature of GaAs amounts to 1240 °C. The inset shows the power profile of the KrF laser. The symbol color is corresponding with the line color in the main panel.

After 26 ns the temperature is highest at the sample surface. The maximum extension of the liquid layer is reached after the laser pulse. The time duration in the liquid phase is strongly correlated with the applied energy density.[27] The structural properties will depend strongly on the thickness of the molten layer. If the liquid-solid interface reaches its maximum extension in the unimplanted crystalline GaAs bulk material, nearly perfect regrowth may start from crystalline bulk GaAs. If the molten layer does not exceed the implanted GaMnAs layer, the recrystallization starts from differently oriented recrystallization seeds in the implanted amorphous GaMnAs and results in a polycrystalline regrowth near the maximum melting depth. The influence of the black body radiation emitted by the sample can be neglected. At approximately 1500 °C the emitted power amounts to only 28 W for a 0.5 cm^2 large sample area and is much smaller than the laser power of around 380 kW at 40 ns. Here we also neglect the convective flow of heat. In summary, only the diffusive energy transfer into the sample is important. Furthermore, because of the relatively low energy deposition of 130 mJ on an area of 0.5 cm^2, the calculated temperature would not increase more than 250 K over the melting temperature. Therefore, the calculated temperature profile for deeper regions and after longer times (0.1 μs) should be correct. After 100 ns the temperature in the implanted layer amounts to only 600 °C and after 1 μs to only 200 °C. This is the typical temperature at which no phase separation occurs in LT-MBE grown GaMnAs samples. In general, the presented semianalytical model is valid for small melting depths. Deeper melting leads to a long recrystallization process and the latent heat is extending the complete cooling process. However, we point out that for a lot of "exotic" semiconductors, the basic thermodynamic material parameters are widely scattering or even not available in literature. Therefore, it is hard to perform more accurate numerical calculations for a lot of highly implanted semiconductors.

For a FWHM pulse length of around 30 ns, the threshold laser fluences for melting amorphous and crystalline GaAs are 80 mJ/cm^2 and 220 mJ/cm^2, respectively.[4] The Nd:YAG laser used in our experiment is also sufficient to melt an approx. 100 nm thick Mn-implanted GaAs layer or even more. The shorter pulses of 3–5 ns lead to an increasing melting depth for the same energy because of the reduced heat flow into the substrate. Unfortunately, the large absorption length can compensate this effect. Note that a ps-laser pulse may create a larger temperature gradient and a higher cooling rate but it is not possible to melt several hundreds of nm GaAs. Nevertheless, the Nd:YAG and the KrF-laser are useful to investigate the PLA dependent magnetic properties of GaMnAs.

In Ref. 28 the absorption length of amorphous GaAs at a wavelength of 1.06 μm (Nd:YAG) is given with 260 nm and at a wavelength of 0.53 μm with 15 nm. The assumption that most of the energy is deposited near the surface in amorphous GaAs is reasonable for the Nd:YAG laser. Due to the higher absorption coefficient of GaAs at the shorter wavelength of the KrF laser, even more of the energy is deposited at the surface during annealing with a KrF laser. Possible calculation errors result from general assumptions. From bulk Si it is known that the thermal diffusity decreases with temperature.[45] That increases the real temperature in comparison to the calculated temperature near the surface. On the other hand there exist compensating effects like the partial reflection of the laser at the sample surface that leads to a lower temperature in comparison to the calculated temperature. For highly doped and damaged crystals only some of the necessary material parameters are available and even in numerical calculations a lot of assumptions have to be made.[17] Therefore, all presented temperature profiles have been calculated with the values of crystalline GaAs. The measured and calculated melting depths are in good agreement. The presented semianalytical calculation allows a relatively easy estimation of the threshold laser fluences for various materials.

Finally, we discuss the potential of one-dimensional (1D) scanning PLA compared to two-dimensional (2D) PLA applied here. The idea behind 1D PLA is the increased cooling rate and the resulting higher activation of dopants. Until now Mn diffusion and clustering after the epitaxial regrowth of the heated up GaMnAs has been neglected. Mainly secondary phase separation in the solid phase has to be prevented because this decreases the amount of substitutional Mn dopants. Therefore, the time period during which the sample remains above a certain temperature after applying the PLA pulse is also a very important parameter.

The phase separation of a diluted system with a fast quenching process was theoretically investigated by Sato *et al.*[29] The attractive forces between Mn ions in GaMnAs or other wide-band-gap materials play an important role.[30,31] We think that the time-dependent temperature profile after one laser pulse also influences the decomposition of such a material system. From a simple point of view, the temperature dependent diffusion coefficient in the solid phase is described by $D_0 \exp(\frac{-Q}{kT})$, where Q refers to the diffusion barrier height.[32] This indicates that with small energy density variations and at higher temperatures during PLA the material properties can also be largely influenced by possible secondary phase separation. Therefore, reducing the entire an-

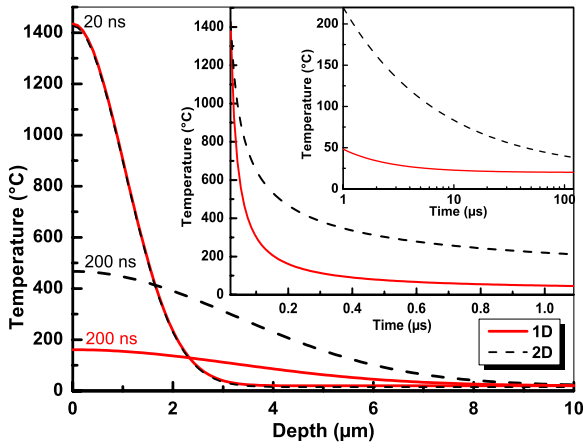

FIG. 2. (Color online) Calculated depth and time-dependent temperature profiles for a single deltalike pulse at t=0. We assumed the same temperature profile at t=20 ns as starting condition for the 1D and 2D heat-flow calculation. The insets show the time-dependent temperature in a typical depth of 100 nm.

nealing process time remains an ongoing issue which can be possibly addressed by 1D scanning PLA. In the case of 1D scanning PLA with an infinitely long and very thin scan stripe in z direction and a δ-function like pulse at $t=0$ the heat-flow equation reads

$$G_0(\vec{r},t) = \frac{1}{4\pi at}\exp\left(\frac{-|\vec{r}|^2}{4at}\right), \tag{7}$$

where $\vec{r}$ lies in the x-y plane of the substrate.

For a better visualization of 1D PLA in comparison to 2D PLA, some calculated temperature profiles are presented in Fig. 2. As the initial condition, the temperature distribution after 20 ns was set to identical values. The thermal diffusivity was chosen from GaAs. Applying Eqs. (3) and (7) for a time of 200 ns shows the main advantage of 1D PLA compared to 2D PLA, i.e., the enhanced cooling rate after a short time of the laser pulse results in a faster cooling process. For example in GaMnAs this temperature should lie below the LT-MBE growth temperature of around 250 °C in order to avoid further phase separation and to remove the easily diffusing Mn interstitials which compensate holes. For material systems with even lower threshold temperatures as determined by higher diffusion coefficients phase separation may be much more pronounced. Temperatures of around 60 °C, can be reached with 1D PLA much faster. Less than 1 μs is needed after a 1D PLA pulse for reaching temperatures of around 60 °C in GaAs in comparison to 20 μs after 2D PLA pulse (inset in Fig. 2). Note that in the case of 1D scanning PLA we have a radial symmetry in z direction. Therefore, the "area" under the graph is not a conserved quantity during the temporal development in this diagram. In Fig. 2 the depth at 0 μm for the 1D scanning PLA corresponds to $x=y=0$ μm.

As a result, 1D PLA allows to improve the incorporation and activation of dopants with the potential use for large scale samples. The physical problem for the 1D scanning PLA is the overlap of neighboring scan stripes that may lead to a decreasing activation of dopant atoms. Therefore, here we also investigated the influence of several PLA pulses on Mn-implanted GaAs.

Also after the laser pulse, two processes in GaMnAs should be considered: Mn diffusion and clustering. During cooling after the PLA pulse the Mn solubility decreases and diffusion of Mn may result in small clusters that decrease the effective hole doping. Diffusion is the only way to reach the thermodynamic equilibrium state after nonequilibrium preparation with PLA or LT-MBE. For the 2D annealing conditions applied here we calculate a Mn diffusion length of 0.1 nm for substitutional Mn in the solid phase that is far away from the mean distance of Mn in GaAs. The vacancy-assisted diffusion mechanism of substitutional Mn plays the major role for clustering processes in GaMnAs.[33] The interstitial diffusion becomes important for long time post growth annealing at lower temperatures. Because of the low diffusion length of substitutional Mn, the possibility of Mn clustering during 2D annealing of Mn-implanted GaAs is low. An extreme example is the long time annealing of LT-MBE grown samples above their growth temperature that leads to the formation of ferromagnetic MnAs clusters with a Curie temperature T_C of 310 K.[20–23] Note, that the Mn diffusion in the liquid phase is much higher, and expected to be not so important for the clustering of dopants. The reason is the higher solubility in the liquid phase that prevents clustering processes. The equilibrium conditions of GaMnAs at room temperature for Mn doping concentrations that are necessary to create a diluted ferromagnetic semiconductor are characterized by separated phases. The time to reach the equilibrium state at room temperature depends strongly on the Mn diffusion coefficient and lies in the order of $>10^{10}$ years in GaMnAs ($t=L^2/D$ with $D=6.5\times10^{-5}$ $\frac{\mathrm{m}^2}{\mathrm{s}}\exp(\frac{-2.5\ \mathrm{eV}}{0.026\ \mathrm{eV}})$ and $L\approx$ nm). At elevated temperatures the equilibrium state can be reached much faster than at low temperatures. For other combinations of materials the diffusion coefficient at room temperature can exceed critical values and phase separation occurs on much shorter time scales. For example, Mn in Si diffuses much faster and the equilibrium state of Si:Mn is reached within several seconds at room temperature ($D_0=6.9\times10^{-8}$ $\frac{\mathrm{m}^2}{\mathrm{s}}$, $Q=0.63$ eV). The reported silicide formation in literature is the direct evidence for the discussed thermodynamic picture.[34,35] Therefore, there exists a thermodynamical limit which is independent of the preparation technique and strongly dependent on the diffusion coefficient. This limit prevents the operation of several metastable ferromagnetic semiconductors at room temperature, e.g., Mn doped Si.

In summary, we presented a short overview over the time-dependent heat-flow characteristics after a ns-laser pulse. Not only the pulse length but also the size of the laser beam play an important role in the cooling process. Fast cooling down the sample after liquid phase epitaxy is essential. Otherwise the sample material tends to cluster and deactivation processes occur if the magnetic dopant concentration lies over the solid solubility limit.

IV. STRUCTURAL PROPERTIES

In order to correlate structural and magnetic properties, we investigated the recrystallization after one and ten PLA

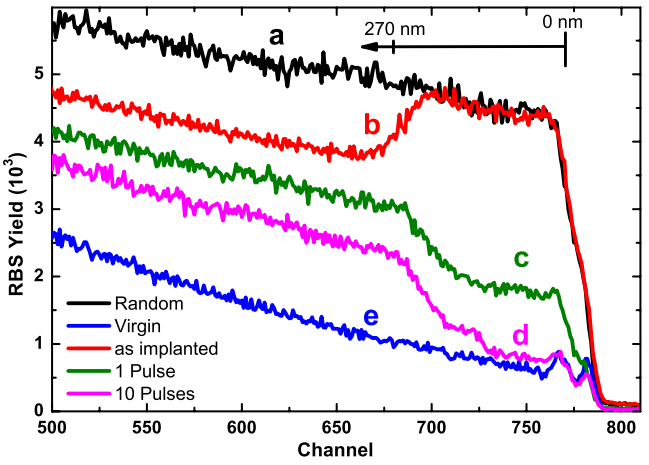

FIG. 3. (Color online) RBS spectra of the implanted sample with 6 at. % Mn. a—random spectrum for a virgin sample, and channeling spectra: b—as-implanted, c—PLA with one pulse, d—PLA with ten pulses and e—channeling spectrum of the virgin sample.

pulses by means of RBS/C, PAS and HRXRD measurements. Basically, an incomplete recrystallization has been proven by RBS and PAS and it seems that the sensitive and nondestructive PAS technique will become the technique of choice for probing the depth distribution of vacancies after PLA. This is from general interest because liquid phase epitaxy can create vacancy-type defects that reduce the Curie temperature in GaMnAs.

A. RBS

The imperfect recrystallization of the implanted GaMnAs layer after PLA can be investigated by depth dependent RBS/C measurements. The crystalline quality can be characterized by χ_{min}, the channeling minimum yield in RBS/C measurements. χ_{min} is the ratio between the backscattering yield at channeling conditions and the backscattering yield for a random beam incidence.[36] Therefore, χ_{min} labels the lattice disordering degree upon implantation. An amorphous sample exhibits a χ_{min} of 100%, while a perfect single crystal corresponds to a χ_{min} of 1–2%. The channeling spectra were collected by aligning the sample to make the impinging He^+ beam parallel with the GaAs⟨001⟩ axis. In Fig. 3 selected RBS spectra are plotted to compare the recrystallization after PLA.

After implantation of Mn, the 270 nm thick top layer reveals the expected amorphouslike structure. This is verified by a comparison between the random spectrum (labeled "a") and the channeling spectrum of the as-implanted sample (labeled "b"). Both spectra overlap with each other in the top layer of around 270 nm, corresponding to χ_{min} of 100%. The virgin GaAs shows clearly channeling behavior ("e"), with two surface peaks at channel Nr. 765 and Nr. 780 corresponding with the energy of He^+ ions scattered at Ga and As atoms from the surface, respectively. After annealing with one laser pulse ("c"), the surface structure changed to crystalline character with a χ_{min} of 40%. The channeling character of the sample becomes even better after ten pulses, which is reflected by a further decrease of χ_{min} to 19% ("d"). However, in both annealed samples the RBS yield is increasing from channel 725 to 675. This channel numbers are related with depths from around 150 to 270 nm. It is due to the melting depth limitation that in this regions no liquid phase epitaxy occur and at lower temperatures (as shown in Fig. 1) the solid phase recrystallization is not effective. Mostly, the transition area between the deep amorphous region and the crystalline surface region have polycrystalline character. Note that in the work of Scarpulla *et al.*,[4] after PLA with one pulse the implanted region is almost completely recrystallized and has a χ_{min} comparable to a virgin GaAs wafers. This is due to the higher pulse energy of 0.41 J/cm^2 and the complete melting of the 250 nm thick implanted GaAs layer in Ref. 4.

B. PAS

Using PAS it is possible to analyze the depth distribution of vacancy-type defects.[37] Especially after the imperfect recrystallization, many vacancies should lie in the range of the maximum melting depth. PAS measurements were carried out with the monoenergetic positron beam "SPONSOR" at Rossendorf[38] at which a variation of the positron energy from 30 eV to 36 keV is possible. The energy resolution of the Ge detector at 511 keV is (1.09 ± 0.01) keV, resulting in a high sensitivity toward changes in material properties from surface to depth. About 5×10^5 events per spectrum were accumulated.

The motion of the electron-positron pair prior to annihilation causes Doppler broadening of the 511 keV annihilation line and can be characterized by the line-shape parameter S. In brief, the value of S is defined by the ratio of counts in the central region of the annihilation gamma peak to the total number of counts in the peak. It is common to define the central region for a certain material to obtain $S_{bulk}=0.5$ for a perfect GaAs reference sample. Then a S-parameter higher than 0.5 (or $S/S_{bulk}>1$) refers to vacancy-type defects in the sample due to the more likely annihilation of positrons with low momentum electrons in this region. For a more general discussion of the S-parameter we refer to Refs. 37 and 39. Figure 4(a) shows the energy-dependent depth profile (Makhov distribution) of the implanted positrons. By assuming such Makhov profiles it is possible to fit a box-shaped, depth-depending layer structure from the S(E) curves using the software package "VEPFIT."[40] In Fig. 4(b) the $S(E)$ curve and the fitted layer structure of a virgin GaAs sample are shown. A damaged layer with a thickness of (49 ± 18) nm on top of the sample is visible. The $S/S_{bulk}=1.02$ of the deeper bulk material is a little bit higher than that one for the reference sample. This might be caused by negatively charged Zn acceptors. After ion implantation three different layers can be detected as shown in Fig. 4(c). The highly destroyed layer of (33 ± 22) nm on top of the sample is the result of the further damage of the thin surface layer mentioned above. The observed As loss at the surface after implantation surely contributes to this damage. The following deeper lying region between 33 and 240 nm characterizes the open-volume defects created by Mn implantation.

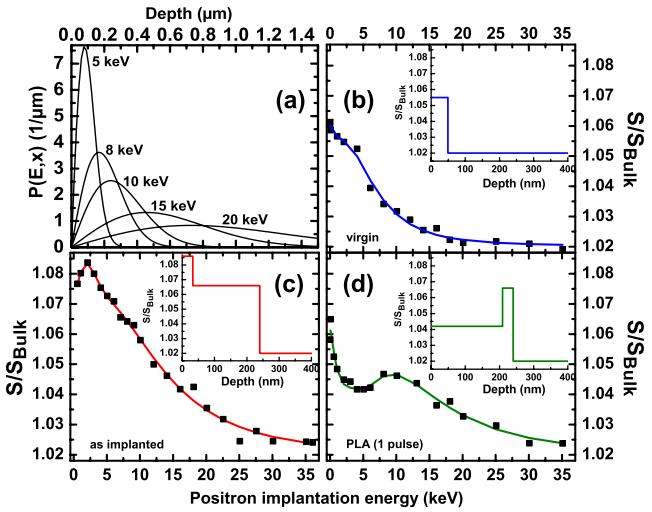

FIG. 4. (Color online) (a) Distribution of the implanted positrons for some selected positron energies. PAS-spectrum of the virgin sample (b) the implanted sample with 6 at. % Mn (c), and the sample annealed with a single KrF-pulse (d)

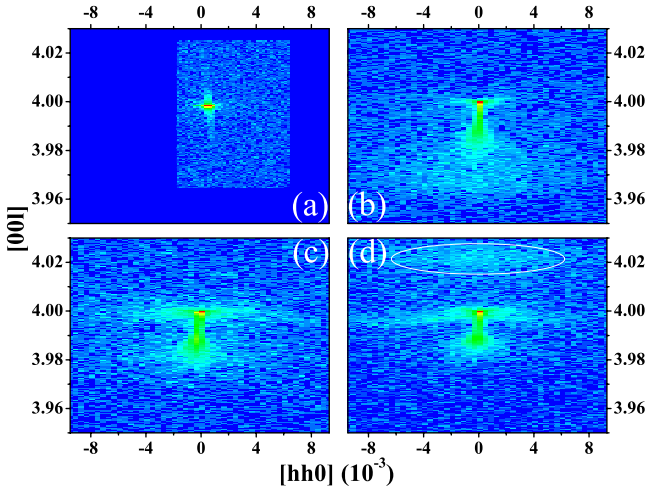

FIG. 5. (Color online) RSM of the (004)-reflection of (a) virgin GaAs, (b) GaAs implanted with 3 at. % Mn, (c) annealed with one pulse and (d) annealed with ten pulses.

It is in agreement with the amorphouslike structure observed by RBS (Fig. 3). Finally, the bulk material is reached at a depth of 240 nm. PLA changed the layer structure in a region down to 210 nm as demonstrated in Fig. 4(d). The highly damaged layer with a thickness of 33 nm on top disappeared and the new first recrystallized topmost layer is extended down to a depth of (209 ± 53) nm. The S/S_{bulk} ratio of this layer amounts to 1.042 and is lower than that of the remaining implanted region between 209 and 240 nm. That means that down to a depth of about 209 nm a decrease of the vacancy-type defects has been probed. However, the laser energy was not high enough in order to melt the whole implantation region. If the molten layer does not penetrate the implanted region, solidification starts from the seeds of the remaining amorphous implantation region. The solidification of the molten layer led to an incomplete and flawed recrystallization. This is reflected by the high S-parameter. In this transition area, TEM images show big crystals with different orientations.

C. HR-XRD

Extensive structural analysis and TEM measurements were carried out by Moreno *et al.* on synthesized ferromagnetic MnAs particles in LT-MBE grown GaMnAs after long time annealing above the growth temperature.[20–23] In our case, a longer annealing time of Mn-implanted GaAs was "simulated" with ten laser pulses at a frequency of 1 Hz. One second is enough time to cool down the sample to room temperature (Fig. 2). SQUID measurements do not give hints for ferromagnetic MnAs cluster formation. Therefore, as the next step in our experiment high resolution x-ray diffraction (HR-XRD) and reciprocal space mapping (RSM) were carried out on the 3 and 6 at. % sample and provided mainly similar information about lattice constant, strain, relaxation, and crystalline perfection related to the dislocation density, mosaicity, and composition. In Fig. 5 the RSM of the symmetrical (004)-reflex of the 3 at. % sample is presented. From the (004)-reflex of the virgin sample [Fig. 5(a)] one can conclude that the MOCVD-grown GaAs film has a good structural quality, as there is almost no broadening of the GaAs substrate peak. The Mn implantation for 3 at. % [Fig. 5(b)] and 6 at. % (not shown here) causes a damaged strained layer that is located close to the surface. The broadening of the GaAs substrate peak after implantation can be attributed to the damaged surface. The implantation leads to a lattice expansion only perpendicular to the sample surface; this was proven by measuring the asymmetric (224) reflex. The lattice expansion perpendicular to the surface was determined by the simulation program RCREFSIMW version 1.09 (not shown). The thickness of the strained layer amounts to 140 nm for 3 at. % and to 280 nm for 6 at. % Mn implantation. In addition, a single laser pulse annealing causes a slight relaxation of the system [Fig. 5(c)]. The ten pulse laser annealing does not return the system to its initial unstrained state. But at $l=4.02$, i.e., at higher 2θ values, an additional weak peak appears [Fig. 5(d)]. The calculated distance between two adjacent planes for this peak does not differ strongly from $d_{004}=1.413$ Å for the GaAs substrate and its value corresponds to $d_{hkl}=1.406$ Å (for both cases). If we interpret the implanted and annealed layer as an area consisting of perfect but strained mosaic blocks separated by a dislocation network, this peak can be attributed to almost randomly compressively strained crystallites inside the dislocation network which compensate the strain caused by implantation. It should be noted that the RSM peak at $l=4.02$ [Fig. 5(d)] corresponds as well to the (202) hexagonal MnAs lattice constant. But additional x-ray investigations did not reveal any other reflections of randomly oriented hexagonal MnAs.

In this section the structural properties of GaMnAs have been presented. The RBS and PAS results indicate a recrystallized, ca. 120–150 nm thick GaMnAs top layer. Below this layer a slowly increasing RBS yield indicates a transition layer with increasing number of structural defects. The fitting results of the PAS measurements hint toward many defects in

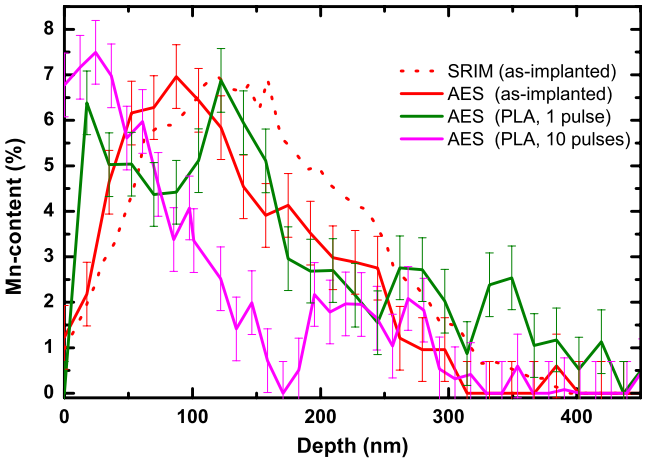

FIG. 6. (Color online) Simulated and experimentally observed implantation profile for the as-implanted 6 at. % sample and the 6 at. % samples annealed with one and ten KrF-excimer-laser pulses. The largest surface segregation of Mn is visible after ten pulses.

the depth from 210 to 250 nm. It seems that in the unimplanted region below 300 nm the heat during the PLA process does not create any damage in bulk GaAs. The XRD results show a continuously strained layer after implantation. In LT-MBE grown GaMnAs on GaAs there exists one additional peak for lower l which represents the larger lattice parameter of GaMnAs.[41] After implantation and PLA the inhomogeneous Mn distribution leads to a XRD (004) reflection which continuously changes between $l=3.98$ and 4.00. After ten pulses the probed additional overcompensation represents an increasing imperfection of the lattice.

V. MAGNETIC PROPERTIES

In the following, the magnetic properties of Mn-implanted GaAs after PLA with different pulse duration and pulse number will be discussed. Briefly, annealing with a single KrF laser pulse of 30 ns and 0.26 J/cm^2 with the photon energy above the GaAs band gap energy leads to similar magnetic properties like annealing with a single 3 ns Nd:YAG laser pulse with the photon energy below the GaAs band gap energy. We observed that possibly due to Mn diffusion and decreasing hole concentration, several laser pulses degrade the structural and magnetic properties of GaMnAs.

The results from Auger electron spectroscopy (AES) measurements and from the corresponding SRIM2008 simulations[46] (Fig. 6) reveal that the magnetic layer is not boxlike homogeneous. The SRIM calculation neglects sputtering effects. The shift of the AES spectrum from the as-implanted sample with respect to the simulated Mn profile amounts to approximately 40 nm and clearly shows that sputtering effects cannot be neglected. Furthermore, with increasing number of PLA pulses Mn tends to segregate to the surface. One PLA pulse is enough to realize a relatively homogeneous Mn distribution over the topmost 150 nm. The maximum Mn content after one PLA pulse is detected close to the surface at a depth of 120 nm. Nearly no Mn is lost

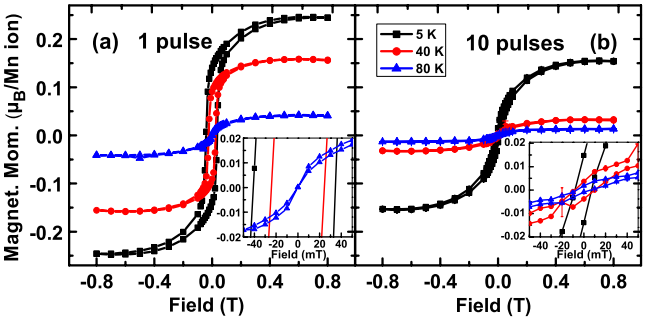

FIG. 7. (Color online) Hysteresis loops of the 6 at. % PLA sample measured at 5, 40, and 80 K. (a) one pulse. (b) ten pulses. The insets show the region near the origin.

after one pulse, but a relatively large amount of Mn was detected in a depth of around 340 nm. This is possibly due to a small channeling effect during implantation in this sample. After ten pulses around 20 % of the Mn is lost and the maximum peak lies at 25 nm. The estimated Mn diffusion coefficient under PLA conditions amounts to approx. 10^{-7} m^2/s being seven orders of magnitudes higher than the expected diffusion coefficient at 1500 K.[42]

A. SQUID magnetometry

The magnetic properties have been investigated by means of SQUID and magnetotransport measurements. Using SQUID it is possible to measure the entire magnetic moment of the sample. With magnetotransport it is possible to measure the anomalous Hall effect (AHE) in the current transporting layer. If the sample is not homogeneous, there should exist differences in the shape of the SQUID and AHE hysteresis loops.

We carried out hysteresis loop measurements and temperature dependent saturation magnetization measurements. All SQUID results are normalized with respect to the number of implanted Mn ions. The diamagnetic background has been subtracted by fitting the linear part in the high-field region. Figure 7 shows in-plane loops probed at 5, 40, and 80 K on the 6 at. % sample annealed with one and ten laser pulses.

It is clearly visible that with increasing temperature the saturation magnetization decreases. The magnetic moment reaches only values up to $0.25\mu_B$ per implanted Mn ion, much smaller than the value in LT-MBE samles. It is due to the fact that the energy of the single laser pulse was not enough to anneal the entire implanted 300 nm thick layer as evidenced by our heat-flow calculation and by RBS/C measurements (Sec. IV A). The microstructure of the as-implanted layer shows dislocation lines and polycrystalline regions. These characteristics were not removed completely in the non molten layer after PLA. After applying ten laser pulses the saturation magnetization at 5 K decreases by 40% [Fig. 7(b)]. This is more than it can be expected from the Mn lost at the surface after annealing with ten laser pulses. Moreover, annealing with one pulse induces a large coercivity of around 400 Oe at 5 K while annealing with ten pulses leads to a strong reduction of coercivity (insets in Fig. 7).

We also probed the hysteresis loops on the 3 at. % Mn sample annealed with one, ten, and 100 pulses. With increas-

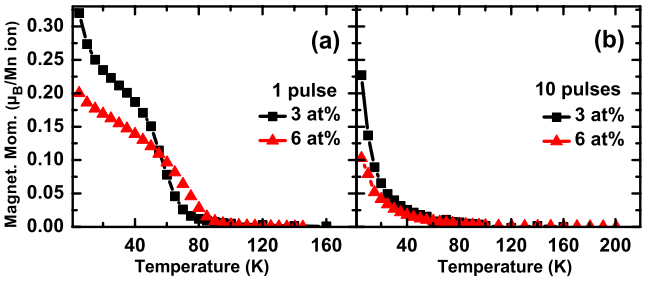

FIG. 8. (Color online) Temperature dependent magnetic moment probed at a field of 0.1 T on samples implanted with 3 and 6 at. % Mn and annealed with one (a) and ten laser pulses (b). The diamagnetic background has been subtracted.

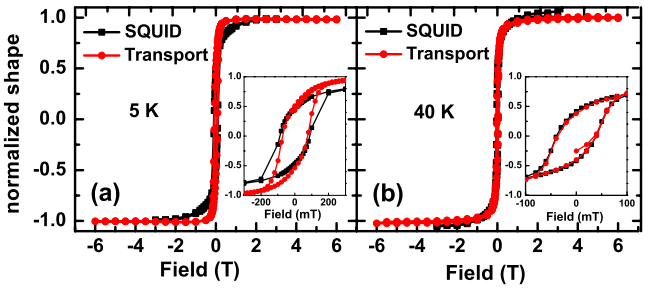

FIG. 9. (Color online) Magnetotransport and SQUID data (out-of-plane) at 5 K (a) and 40 K (b) of the 6 at. % sample annealed with one KrF laser pulse normalized with respect to the saturation values. There is a clear correlation between magnetization and anomalous Hall resistance. The inset shows the shape near the origin.

ing number of laser pulses the saturation magnetization decreases like in the 6 at. % sample. After 100 pulses the magnetic susceptibility, coercivity, and remanence have very low values (not shown here). The reduced ferromagnetic properties are also visible in the $M(T)$ measurements. The magnetization of the ten pulses samples strongly decreases with increasing temperature [Fig. 8(b)] in comparison to the one pulse samples [Fig. 8(a)]. At temperatures higher than 120 K, no additional drop in the magnetization is visible, especially in the ten pulses sample, where the risk for the build up of ferromagnetic phases is much higher. Therefore, the formation of ferromagnetic MnAs precipitates seems to be prevented. The one pulse samples have higher Curie temperatures of 70 K for the 3 at. % and 85 K for the 6 at. % Mn implantation. The SQUID results also indicate a stronger paramagnetic interaction.

In order to investigate the influence of the PLA conditions we annealed samples with 3 at. % Mn also with one Nd:YAG laser pulse. Due to the longer wavelength of the Nd:YAG laser, the absorption length increases to 260 nm in amorphous GaAs.[28] This effect reduces the temperature gradient in the sample during annealing. On the other hand, the relatively short energy deposition time of 3–5 ns should heat up the implanted layer faster. Both parameters have a compensating effect on the temperature gradient and therefore on the cooling rate.

After Nd:YAG annealing all samples show clear ferromagnetic hysteresis loops. We found no significant difference (not shown) in the Curie temperature compared to the sample annealed with one KrF-excimer laser pulse [Fig. 8(a)]. The higher power density of the Nd:YAG laser only leads to a deeper melting and a larger magnetic moment. Therefore, we conclude that the free hole concentration is not increased after applying the Nd:YAG laser annealing. The influence of the energy density, thickness of the molten layer, wavelength of laser light, absorption length, and resulting cooling rate on the magnetic and electric activation has to be clarified in further detailed investigations.

B. Magnetotransport

Magnetotransport measurements have been performed on samples in the van-der-Pauw geometry. The field was applied perpendicular to the sample surface. From the AES measurements (Fig. 6) we know the depth of the layer with the largest Mn concentration and presumably also with the largest hole concentration. At 290 K the unimplanted Zn-doped layer has a sheet resistance of 38 kΩ and was not measurable at low temperatures. Therefore, we assume that the highly resistive Zn-doped GaAs layer underneath the Mn-implanted GaAs layer has no influence on the transport properties. The top GaMnAs layer with the largest hole concentration mainly determines the magnetotransport properties. In the following we compare the shape of the magnetization and the Hall resistance under the assumption that the ordinary Hall resistance is negligible. In Fig. 9 the 5 and 40 K hysteresis are presented. It is clearly visible that at 40 K the magnetization and the anomalous Hall effect hysteresis are strongly correlated with each other. There exists a small difference at 5 K in the hysteresis shape [Fig. 9(a)]. This can be attributed to slightly different current paths at 5 K. At 40 K the SQUID and AHE hysteresis reveal the same hysteresis shape [Fig. 9(b)]. From that we conclude that the magnetization probed by SQUID is due to hole-mediated ferromagnetism related with free holes and localized magnetic moments in the current transporting GaMnAs layer. Thus, it is clearly visible that implantation with subsequent pulsed laser annealing is a possible technique to create a GaMnAs DMS with similar transport properties as for homogeneously grown LT-MBE GaMnAs.[7,8]

In the next step, we measured the Hall resistance [Fig. 10(a)] and MR [Fig. 10(b)] at different temperatures. In Fig. 10(a) the Hall resistance of the 1 pulse sample is presented. The hysteresis of the Hall resistance is visible at 5 and 40 K, but not at 80 K. The Hall resistance of the ten pulses sample at 5 K (not shown here) is ten times larger than for the 1 pulse sample possibly due to its lower effective hole concentration. Structural defects or other limitations may also decrease the hole scattering time and therefore the measured Hall voltage. Especially, in the regime above the Curie temperature at 120 and 300 K the Hall resistance is around three times larger for the ten pulses sample. The reduced sheet hole concentration (Table II) explains the observed lower Curie temperature and is in good agreement with the Zener model. Note that the sheet hole concentration is underestimated because a possible paramagnetic background may cause a higher Hall resistance and therefore a lower hole

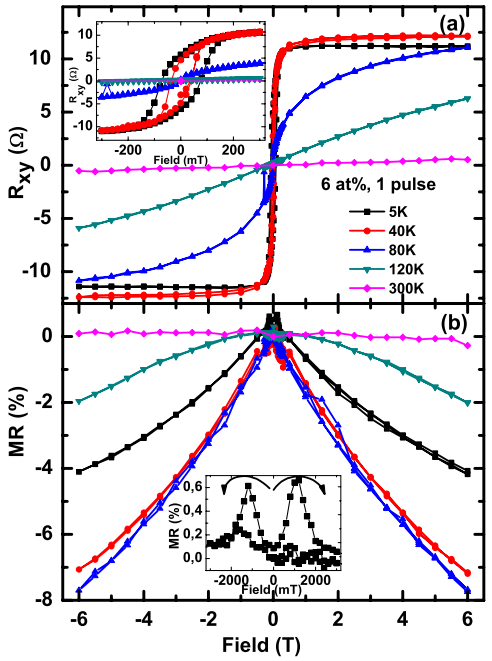

FIG. 10. (Color online) (a): Hall resistance and (b) magnetoresistance of the 6 at. % PLA sample annealed with one laser pulse measured at 5, 40, 80, 120, and 300 K. The insets show the region at low field in more detail.

concentration calculated from the measurement results. The typical negative magnetoresistance for ferromagnetic GaMnAs can be reproduced after one pulse and is shown in [Fig. 10(b)]. In comparison to that, the MR of the ten pulses sample at 5 and 40 K (not shown here) amounts to 20% at a field of 6 T. We explain the strongly decreased resistance at high fields with the reduced scattering of spin polarized holes at localized Mn ions if their magnetic moments are aligned at high fields. Above the Curie temperature (120 and 300 K) the MR is similar for the one pulse sample [Fig. 10(b)] and the ten pulses samples. This indicates that magnetic properties play a fundamental role in the magnetoresistance of GaMnAs.

Figure 11 represents the temperature dependent resistivity of the 6 at. % one pulse and ten pulses samples. The resistivity of the sample annealed with one pulse reaches its maximum at the Curie temperature amounting to 80 K. This behavior is already known from the LT-MBE samples and is explained by the misalignment (spin fluctuation) of Mn ions and the resulting maximum scattering at the Curie temperature. The increasing resistivity at temperatures below 15 K is also an effect known from LT-MBE samples. The Kondo

TABLE II. Sheet carrier concentration in units of cm^{-2} and mobility in units of cm^2/V s of the PLA annealed samples implanted with 6 at. % Mn at 300 K

PLA sample	Sheet carrier conc. (cm^{-2})	Mobility (cm^2/V s)
1 pulse	7×10^{15}	3.0
10 pulses	2.4×10^{15}	2.9

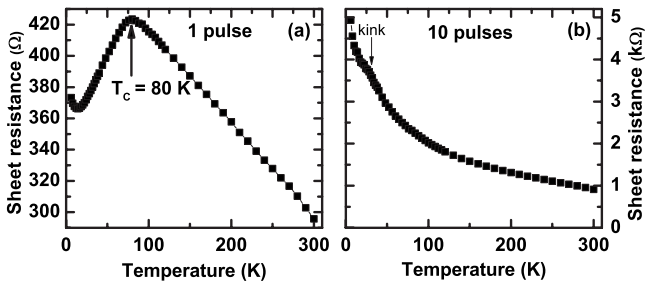

FIG. 11. Sheet resistance of the 6 at. % PLA sample annealed with (a) one laser pulse and (b) with ten laser pulses.

effect[43] or electron-electron interactions have been ascribed to this resistivity behavior.[44] The ten pulses sample reveals a monotonically decreasing resistivity with increasing temperature. Only a small kink is visible at around 25 K having probably the same origin like for the 1 pulse sample at T_C, only in a strongly reduced manner. In general, the decreasing resistivity with increasing temperature is a typical semiconductor transport property, but different fittings to the experimental data do not reveal a certain conduction mechanism. However, the large influence of the Mn ions on the transport properties in GaMnAs is clearly evident.

In this section the magnetic properties of GaMnAs samples annealed under different conditions have been discussed. The samples annealed with one laser pulse show the best magnetic properties. After ten pulses, i.e., after ten subsequent heating and solidification processes, the hole concentration in GaMnAs is reduced. Further investigations have to point out if the hole concentration monotonously decreases as a function of the number of PLA pulses.

VI. CONCLUSIONS AND OUTLOOK

In this paper we investigated Mn-implantion into GaAs followed by PLA using a KrF or a Nd:YAG laser. Our results show that the PLA parameters have to be chosen carefully. A single short PLA pulse creates a GaMnAs DMS, but several laser pulses degrade the magnetic and structural properties of GaMnAs. Also secondary effects like the loss of As during Mn implantation in GaAs may degrade the properties of GaMnAs. The epitaxial regrowth at the liquid-solid interface and the depth and time-dependent temperature profile in the solid phase are the most important parameters that influence the magnetic and structural properties of Mn-implanted GaAs after PLA. Further developments of the PLA technique can make magnetic ion implantation followed by pulsed laser annealing another candidate for the synthesis of new metastable DMS systems. For example even higher cooling rates can be achieved by means of 1D scanning PLA and open the way to create new metastable DMS that cannot be prepared by means of LT-MBE or by magnetic ion implantation followed by the established 2D PLA. However, the degree of magnetic ion dilution in bulk semiconductors represents a thermodynamic limit because the diffusion of magnetic ions in metastable DMS systems leads to unwanted

secondary phase formation. For example the large and small diffusity of Mn ions in the solid phase of metastable Si:Mn and GaMnAs leads to unwanted phase separations on a time scale of several seconds or more than billion years, respectively. Therefore, GaMnAs is metastable-robust for practical spintronics purposes.

ACKNOWLEDGMENTS

The authors (D.B. and S.Z.) thank financial funding from the Bundesministerium für Bildung und Forschung (Grant No. FKZ13N10144). We thank also Matthias Michler for fruitful discussions on the heat-flow modeling.

*d.buerger@fzd.de

[1] J. De Boeck, R. Oesterholt, A. V. Esch, H. Bender, C. Bruynseraede, C. V. Hoof, and G. Borghs, Appl. Phys. Lett. **68**, 2744 (1996).
[2] P. J. Wellmann, J. M. Garcia, J.-L. Feng, and P. M. Petroff, Appl. Phys. Lett. **71**, 2532 (1997).
[3] D. Bürger, S. Zhou, J. Grenzer, H. Reuther, W. Anwand, V. Gottschalch, M. Helm, and H. Schmidt, Nucl. Instrum. Methods Phys. Res. B **267**, 1626 (2009).
[4] M. A. Scarpulla, O. D. Dubon, K. M. Yu, O. Monteiro, M. R. Pillai, M. J. Aziz, and M. C. Ridgway, Appl. Phys. Lett. **82**, 1251 (2003).
[5] M. A. Scarpulla, B. L. Cardozo, R. Farshchi, W. M. Hlaing Oo, M. D. McCluskey, K. M. Yu, and O. D. Dubon, Phys. Rev. Lett. **95**, 207204 (2005).
[6] M. A. Scarpulla, R. Farshchi, P. R. Stone, R. V. Chopdekar, K. M. Yu, Y. Suzuki, and O. D. Dubon, J. Appl. Phys. **103**, 073913 (2008).
[7] A. Van Esch, L. Van Bockstal, J. De Boeck, G. Verbanck, A. S. van Steenbergen, P. J. Wellmann, B. Grietens, R. Bogaerts, F. Herlach, and G. Borghs, Phys. Rev. B **56**, 13103 (1997).
[8] K. W. Edmonds, R. P. Campion, K. Y. Wang, A. C. Neumann, B. L. Gallagher, C. T. Foxon, and P. C. Main, J. Appl. Phys. **93**, 6787 (2003).
[9] M. A. Scarpulla, P. R. Stone, I. D. Sharp, E. E. Haller, O. D. Dubon, J. W. Beeman, and K. M. Yu, J. Appl. Phys. **103**, 123906 (2008).
[10] Y. J. Cho, M. A. Scarpulla, Y. Y. Zhou, Z. Ge, X. Liu, M. Dobrowolska, K. M. Yu, O. D. Dubon, and J. K. Furdyna, J. Appl. Phys. **104**, 043902 (2008).
[11] R. Farshchi, O. D. Dubon, D. J. Hwang, N. Misra, C. P. Grigoropoulos, and P. D. Ashby, Appl. Phys. Lett. **92**, 012517 (2008).
[12] P. R. Stone, M. A. Scarpulla, R. Farshchi, I. D. Sharp, E. E. Haller, O. D. Dubon, K. M. Yu, J. W. Beeman, E. Arenholz, J. D. Denlinger *et al.*, Appl. Phys. Lett. **89**, 012504 (2006).
[13] R. Farshchi, R. V. Chopdekar, Y. Suzuki, P. D. Ashby, I. D. Sharp, J. W. Beeman, E. E. Haller, and O. D. Dubon, Phys. Status Solidi C **4**, 1755 (2007).
[14] G. E. Jellison, F. A. Modine, C. W. White, R. F. Wood, and R. T. Young, Phys. Rev. Lett. **46**, 1414 (1981).
[15] L. Via and M. Cardona, Phys. Rev. B **34**, 2586 (1986).
[16] R. F. Wood and G. A. Geist, Phys. Rev. B **34**, 2606 (1986).
[17] R. F. Wood and G. E. Giles, Phys. Rev. B **23**, 2923 (1981).
[18] M. von Allmen and A. Blatter, *Laser-Beam Interactions With Materials: Physical Principles and Applications* (Springer-Verlag, Berlin, Heidelberg, New York, 1987).
[19] T. Dietl, H. Ohno, F. Matsukura, J. Cibert, and D. Ferrand, Science **287**, 1019 (2000).
[20] M. Moreno, A. Trampert, B. Jenichen, L. Däweritz, and K. H. Ploog, J. Appl. Phys. **92**, 4672 (2002).
[21] M. Moreno, V. M. Kaganer, B. Jenichen, A. Trampert, L. Däweritz, and K. H. Ploog, Phys. Rev. B **72**, 115206 (2005).
[22] M. Moreno, B. Jenichen, L. Däweritz, and K. H. Ploog, Appl. Phys. Lett. **86**, 161903 (2005).
[23] M. Moreno, A. Trampert, L. Däweritz, and K. H. Ploog, Appl. Surf. Sci. **234**, 16 (2004).
[24] G. Andrä, H. D. Geiler, G. Götz, K. H. Heinig, and H. Wittennek, Phys. Status Solidi A **74**, 511 (1982).
[25] A. G. Cullis, Rep. Prog. Phys. **48**, 1155 (1985).
[26] C. W. White, S. R. Wilson, B. R. Appleton, and J. F. W. Young, J. Appl. Phys. **51**, 738 (1980).
[27] R. Klabes, *Nichtkonventionelle Kurzzeit-Temperverfahren zur Modifizierung der Strukturellen und Elektrischen Eigenschaften von Silizium* (ZfK, Dresden, 1984).
[28] W. Wesch and G. Götz, Phys. Status Solidi A **94**, 745 (1986).
[29] K. Sato, H. Katayama-Yoshida, and P. H. Dederichs, Jpn. J. Appl. Phys., Part2 **44**, L948 (2005).
[30] T. Fukushima, K. Sato, H. Katayama-Yoshida, and P. H. Dederichs, Jpn. J. Appl. Phys., Part 2 **45**, L416 (2006).
[31] K. Sato, T. Fukushima, and H. Katayama-Yoshida, Jpn. J. Appl. Phys., Part 2 **46**, L682 (2007).
[32] K. W. Edmonds, P. Bogusławski, K. Y. Wang, R. P. Campion, S. N. Novikov, N. R. S. Farley, B. L. Gallagher, C. T. Foxon, M. Sawicki, T. Dietl *et al.*, Phys. Rev. Lett. **92**, 037201 (2004).
[33] H. Raebiger, M. Ganchenkova, and J. von Boehm, Appl. Phys. Lett. **89**, 012505 (2006).
[34] S. Zhou, K. Potzger, G. Zhang, A. Mücklich, F. Eichhorn, N. Schell, R. Grötzschel, B. Schmidt, W. Skorupa, M. Helm *et al.*, Phys. Rev. B **75**, 085203 (2007).
[35] N. Peng, C. Jeynes, M. J. Bailey, D. Adikaari, V. Stolojan, and R. P. Webb, Nucl. Instrum. Methods Phys. Res. B **267**, 1623 (2009).
[36] W. K. Chu, J. W. Mayer, and M. A. Nicolet, *Backscattering Spectrometry* (Academic, New York, 1978).
[37] R. Krause-Rehberg, *Positron Annihilation in Semicond* (Springer-Verlag, Berlin, Heidelberg, 1999).
[38] W. Anwand, H. R. Kissener, and G. Brauer, Acta Phys. Pol. A **88**, 7 (1995).
[39] A. Dupasquier and A. P. Mills, *Positron Spectroscopy of Solids* (IOS, Amsterdam, 1995).
[40] A. van Veen, H. Schut, J. de Vries, R. A. Hakvoort, and M. R. Ijpma, *Positron Beams for Solids and Surfaces* (AIP, New York, 1990).
[41] L. X. Zhao, R. P. Campion, P. F. Fewster, R. W. Martin, B. Y. Ber, A. P. Kovarsky, C. R. Staddon, K. Y. Wang, K. W. Edmonds, C. T. Foxon *et al.*, Semicond. Sci. Technol. **20**, 369 (2005).
[42] O. Koskelo, J. Raisanen, F. Tuomisto, and J. Sadowski (the

ISOLDE collaboration), Semicond. Sci. Technol. **24**, 045011 (2009).
[43] H. T. He, C. L. Yang, W. K. Ge, J. N. Wang, X. Dai, and Y. Q. Wang, Appl. Phys. Lett. **87**, 162506 (2005).
[44] D. Neumaier, M. Schlapps, U. Wurstbauer, J. Sadowski, M. Reinwald, W. Wegscheider, and D. Weiss, Phys. Rev. B **77**, 041306(R) (2008).
[45] http://www.ioffe.rssi.ru
[46] J. Ziegler, J. P. Biersack, and M. D. Ziegler, *SRIM—The Stopping and Ranges of Ions in Matter* (SRIM Co., Chester, 2008)